# High-spin intruder band in <sup>107</sup>In

E. Ideguchi, B. Cederwall, E. Ganioğlu, B. Hadinia, K. Lagergren, T. Bäck, A. Johnson,<sup>2</sup> R. Wyss,<sup>2</sup> S. Eeckhaudt,<sup>3</sup> T. Grahn,<sup>3</sup> P. Greenlees,<sup>3</sup> R. Julin,<sup>3</sup> S. Juutinen,<sup>3</sup> H. Kettunen,<sup>3</sup> M. Leino,<sup>3</sup> A.-P. Leppanen,<sup>3</sup> P. Nieminen,<sup>3</sup> M. Nyman,<sup>3</sup> J. Pakarinen, P. Rahkila, C. Scholev, J. Uusitalo, D. T. Joss, E. S. Paul, 5 D. R. Wiseman,<sup>5</sup> R. Wadsworth,<sup>6</sup> A. V. Afanasjev,<sup>7</sup> and I. Ragnarsson<sup>8</sup> <sup>1</sup>Center for Nuclear Study, the University of Tokyo, Wako, Saitama 351-0198, Japan † <sup>2</sup>Department of Physics, The Royal Institute of Technology, SE-10691 Stockholm, Sweden <sup>3</sup> Department of Physics, University of Jyväskylä, P.O. Box 35, FI-40014 Jyväskylä, Finland <sup>4</sup>CCLRC, Daresbury Laboratory, Daresbury, Warrington WA4 4AD, United Kingdom <sup>5</sup>Oliver Lodge Laboratory, Department of Physics, University of Liverpool, Liverpool L69 7ZE, United Kingdom <sup>6</sup>Department of Physics, University of York, Heslington, York YO10 5DD, United Kingdom <sup>7</sup>Department of Physics and Astronomy, Mississippi State University, Mississippi State, Mississippi 39762, USA

Lund University, P.O. Box 118 SE-221 00 Lund, Sweden
(Dated: October 30, 2018)

<sup>8</sup>Division of Mathematical Physics, LTH,

Abstract

High-spin states in the neutron deficient nucleus  $^{107}$ In were studied via the  $^{58}$ Ni( $^{52}$ Cr, 3p) reactions.

tion. In-beam  $\gamma$  rays were measured using the JUROGAM detector array. A rotational cascade

consisting of ten  $\gamma$ -ray transitions which decays to the  $19/2^+$  level at 2.002 MeV was observed.

The band exhibits the features typical for smooth terminating bands which also appear in rota-

tional bands of heavier nuclei in the  $A\sim100$  region. The results are compared with Total Routhian

Surface and Cranked Nilsson-Strutinsky calculations.

PACS numbers: 23.20.Lv, 24.60.Dr, 23.20.En, 27.60.+j

\*Also at Department of Physics, Faculty of Science, Istanbul University

†Electronic address: ideguchi@cns.s.u-tokyo.ac.jp

2

#### I. INTRODUCTION

The structure of nuclei close to  $^{100}$ Sn has received increasing attention in recent years. Excited states of neutron deficient nuclei with Z $\sim$ 50 are expected to be predominantly of single-particle nature at low spin due to the presence of a spherical shell gap for protons. However, recent experimental and theoretical investigations have elucidated additional important excitation mechanisms, such as magnetic rotation [1], and deformed rotational bands of dipole and quadrupole character exhibiting smooth band termination [2–7]. The diversity of excitation modes in these nuclei make them particularly interesting systems to study.

In the A~100 region, the observation of well-deformed structures are interpreted as being based on 1p-1h [5, 7] and 2p-2h [2–4, 6] proton excitations across the Z=50 closed-shell gap and on the occupation of the intruder  $h_{11/2}$  orbital. These studies have in particular high-lighted the so-called "smooth band termination" phenomenon, following alignment of the valence nucleons outside the <sup>100</sup>Sn doubly-magic core. In the previous studies, levels in <sup>107</sup>In were extended up to I=(33/2) at 6.893 MeV, the last member of a magnetic-dipole band structure [8]. A well deformed intruder structure has been observed earlier in <sup>107</sup>In (see Fig. 23 in Ref. [4]), but its detailed analysis has not been published so far.

In order to further investigate the existence of well-deformed structures in the A $\approx$ 100 mass region, we have obtained new data on the high-spin states of <sup>107</sup>In. In the present work, a rotational band was observed, extending to high angular momentum (> 30 $\hbar$ ). It is connected with the low-lying yrast states via several  $\gamma$ -ray transitions.

A rotational-like level structure in  $^{107}$ In has recently been reported [9]. Although some of the  $\gamma$ -ray transitions are identical to those observed in the present work, the results are generally not in agreement with the results obtained in the present work. The band was not observed to lower spin states and it was not connected to the lower-lying states in  $^{107}$ In.

## II. EXPERIMENTAL DETAILS

The experiment was performed at the JYFL accelerator facility at the University of Jyväskylä, Finland. The  $^{52}$ Cr ions, accelerated by the JYFL K=130 MeV cyclotron to an energy of 187 MeV, were used to bombard a target consisting of two stacked self-supporting foils of isotopically enriched (99.8%)  $^{58}$ Ni. The targets were of thickness 580  $\mu$ g/cm<sup>2</sup> and

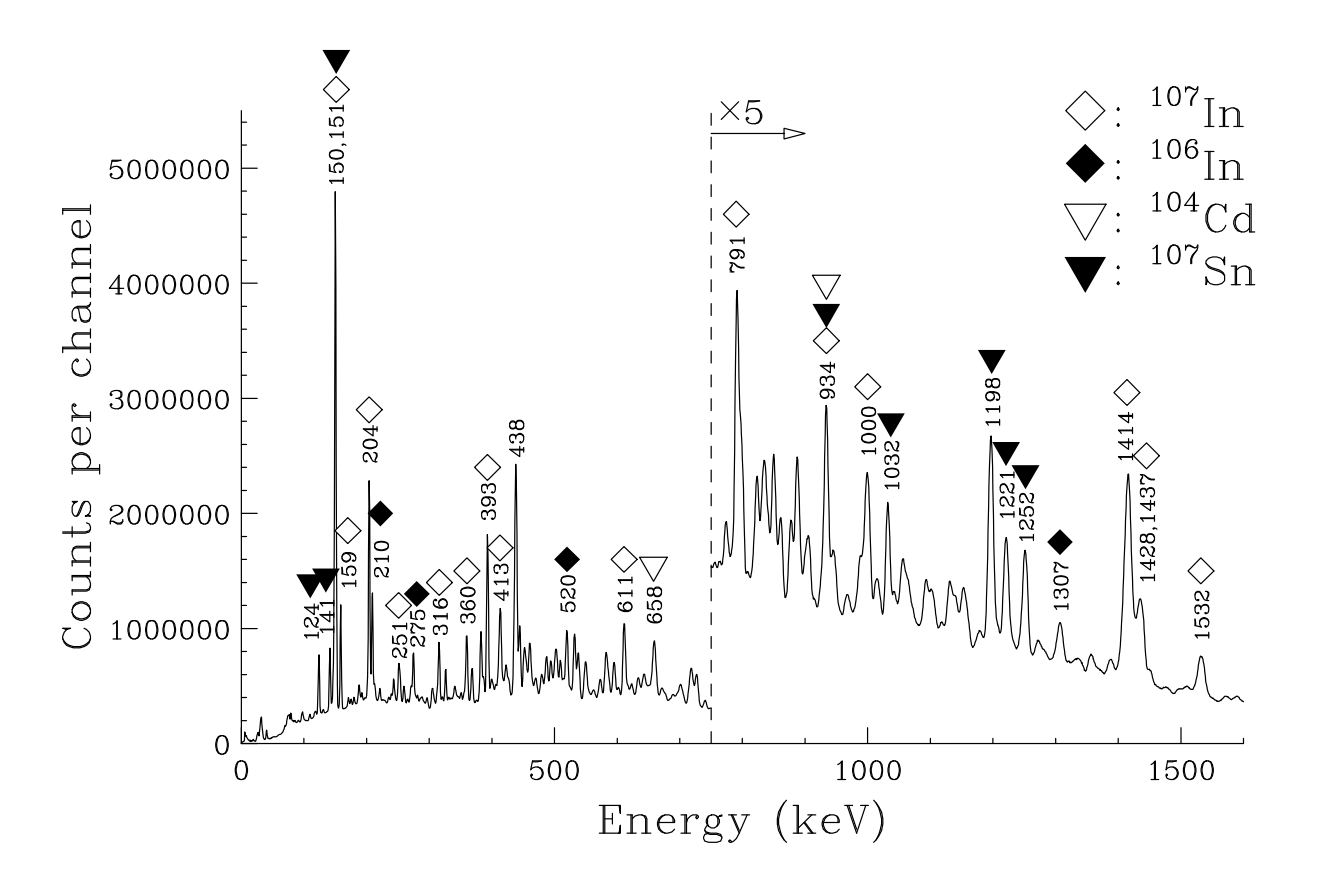


FIG. 1: Total  $\gamma - \gamma$  coincidence spectrum. Gamma-ray peak energies are labeled in keV for strong peaks. Previously known transitions in  $^{107}$ In as well as those from the other principal evaporation residues,  $^{104}$ Cd,  $^{106}$ In, and  $^{107}$ Sn are observed as indicated in the figure.

640  $\mu g/cm^2$ . The average beam intensity was 4.4 particle-nA during 5 days of irradiation time. High-spin states in  $^{107}$ In were populated by the fusion-evaporation reaction  $^{58}$ Ni( $^{52}$ Cr, 3p) $^{107}$ In. Prompt  $\gamma$ -rays were detected at the target position by the JUROGAM  $\gamma$ -ray spectrometer consisting of 43 EUROGAM [10] type escape-suppressed high-purity germanium detectors. In this configuration, JUROGAM had a total photopeak efficiency of about 4.2% at 1.3 MeV. Fig. 1 shows a total  $\gamma - \gamma$  coincidence spectrum. Gamma-ray peaks of  $^{107}$ In are observed as belonging to the strongest fusion-evaporation channel (3p). Other reaction channels such as  $^{104}$ Cd ( $1\alpha 2p$ ),  $^{106}$ In (3p1n), and  $^{107}$ Sn (2p1n) are also observed clearly.

The fusion-evaporation products were separated in flight from the beam particles using the gas-filled recoil separator RITU [11, 12] and implanted into the two double-sided silicon strip detectors (DSSSD) of the GREAT [13] spectrometer. The GREAT spectrometer is a composite detector system containing, in addition to the DSSSDs, a multiwire proportional

counter (MWPC), an array of 28 Si PIN photodiode detectors, and a segmented planar Ge detector. Each DSSSD has a total active area of  $60\times40~\mathrm{mm^2}$  and a strip pitch of 1 mm in both directions yielding in total 4800 independent pixels. In this measurement, GREAT was used to filter the events such that recoils were separated and transported to the final focal plane of RITU.

The signals from all detectors were recorded independently and provided with an absolute "time stamp" with an accuracy of 10 ns using the total data readout (TDR) [14] acquisition system. Events associated with the recoil hitting DSSSD of GREAT and prompt  $\gamma$  rays detected by JUROGAM were sorted offline using GRAIN analysis package [15] to store the recoil-gated multifold  $\gamma$  coincidence data. In total  $5.3\times10^8$  events were accumulated. The data were analyzed using the RADWARE data analysis software package [16]. The multifold event data were sorted offline into an  $E_{\gamma}$ - $E_{\gamma}$  correlation matrix and an  $E_{\gamma}$ - $E_{\gamma}$ -cube. Based on single and double gating on the matrix and cube, respectively, coincidence relations between observed  $\gamma$  rays were examined. Fig. 2 shows a level scheme constructed in the present study.

In order to determine the  $\gamma$ -ray multipolarities, an angular distribution analysis was performed. The germanium detectors of the JUROGAM spectrometer were distributed over six angles relative to the beam direction with five detectors at 158°, ten at 134°, ten at 108°, five at 94°, five at 86°, and eight at 72°. Recoil gated coincidence matrices were sorted such that the energies of  $\gamma$  rays detected at specified angles of JUROGAM,  $E_{\gamma}(\theta)$ , were incremented on one axis, while the energies of coincident  $\gamma$  rays detected at any angles,  $E_{\gamma}(any)$ , were incremented on the other axis. Six angular distribution matrices corresponding to the angles  $\theta = 158^{\circ}$ ,  $134^{\circ}$ ,  $94^{\circ}$ ,  $86^{\circ}$ , and  $72^{\circ}$  were created. Background-subtracted angle-dependent spectra were created by gating on transitions on the  $E_{\gamma}(any)$  of the matrices. Peak areas for a given coincident transition were measured and normalized by the number of detectors as well as efficiencies at each angle, then fitted to the angular distribution function  $W(\theta) = a_0(1 + a_2P_2(\cos\theta) + a_4P_4(\cos\theta))$ . In the case of stretched quadrupole (E2) transitions,  $a_2$  and  $a_4$  coefficients will have positive and small negative values, respectively, while those of pure stretched dipole (M1 or E1) transitions will be negative and zero values, respectively.

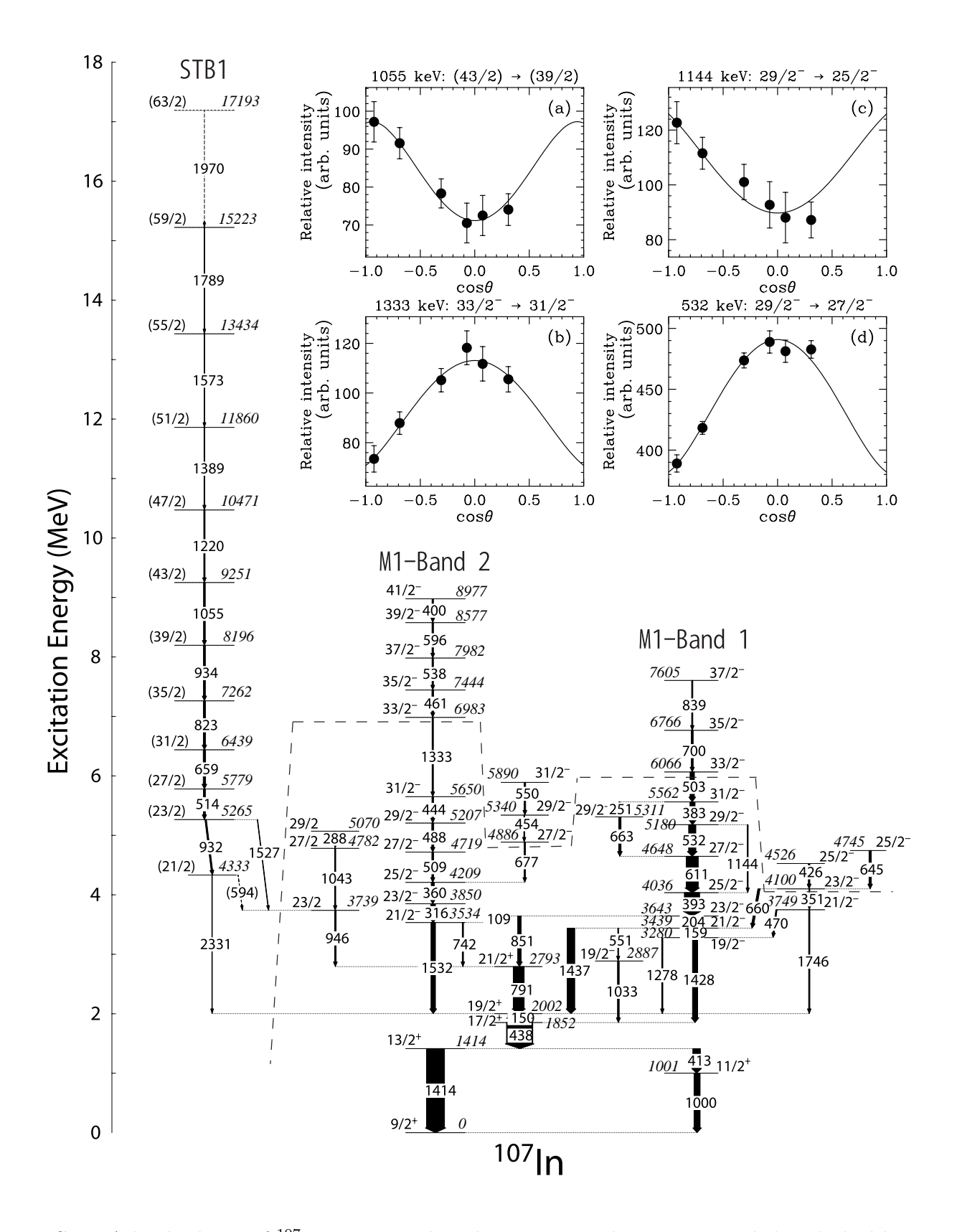


FIG. 2: A level scheme of  $^{107}$ In constructed in the present study. Transitions below dashed lines were previously identified [8]. Insets (a), (b), (c), (d) represent the typical angular distribution of  $\gamma$  transitions observed with present setup. Solid lines are fitted curve of the angular distribution function W( $\theta$ ).

# III. RESULTS

High-spin levels in  $^{107}$ In were previously reported up to the (I=33/2) state at 6.983 MeV excitation energy [8]. The spin-parity of the ground state is  $9/2^+$ , arising from its  $\pi g_{9/2}$  hole character. The  $19/2^+$  state at 2.002 MeV and the  $17/2^+$  state at 1.852 MeV have been reported to have isomeric character with half-lives of 0.6(2) and 1.7(3) ns, respectively [17]. These lifetimes are long enough so that the  $\gamma$ -ray emission depopulating these states or lower-lying states which are fed via these states, on average occurs several cm downstream from the target. This affects the relative efficiency of detecting such  $\gamma$  rays depending on the detector angle relative to the beam and hence their angular distribution. An attenuation of the alignment could also be affected by the level lifetimes. Indeed, the angular distributions of transitions below the state at 1.852 MeV were observed to be isotropic. However, the angular distribution of the 150 keV transition below the 0.6 ns isomer at 2.002 MeV was not isotropic. This is consistent with the fact that the half-life of the isomer is shorter than that of the 1.852 MeV level. The half-lives of these two isomers could not be confirmed in this analysis since the experimental setup was not sensitive for such short lifetimes.

TABLE I: Gamma rays assigned to  $^{107}$ In

$E_{\gamma}{}^{a}$	$I^{(rel.)}\gamma^b$	$E_i{}^c$	$a_2$	$a_4$	$J_i^\pi$	$\rightarrow$	$J_f^\pi$
(keV)		(keV)					
109.3	14(2)	3643	-0.23(17)	0.24(23)	$23/2^{-}$	$\rightarrow$	$21/2^{-}$
149.8	768(48)	2002	-0.260(15)	0.025(22)	$19/2^{+}$	$\rightarrow$	$17/2^{+}$
158.6	183(12)	3439	-0.266(16)	0.003(22)	$21/2^{-}$	$\rightarrow$	$19/2^{-}$
204.0	437(26)	3643	-0.280(15)	0.065(22)	$23/2^{-}$	$\rightarrow$	$21/2^-$
251.2	50(3)	5562	-0.242(47)	0.132(69)	$31/2^{-}$	$\rightarrow$	$29/2^-$
288.4	17(2)	5070	-0.36(12)	0.10(17)	29/2	$\rightarrow$	27/2
315.6	175(12)	3850	-0.224(21)	0.025(31)	$23/2^{-}$	$\rightarrow$	$21/2^{-}$
351.4	33(3)	4100	-0.30(18)	-0.08(28)	$23/2^{-}$	$\rightarrow$	$21/2^{-}$
359.6	115(8)	4209	-0.236(27)	0.010(40)	$25/2^{-}$	$\rightarrow$	$23/2^{-}$
382.9	194(12)	5562	-0.272(14)	0.070(21)	$31/2^{-}$	$\rightarrow$	$29/2^{-}$
393.0	580(36)	4036	-0.219(25)	0.024(37)	$25/2^{-}$	$\rightarrow$	$23/2^{-}$

TABLE I: Gamma rays assigned to  $^{107}\mathrm{In}$ 

$E_{\gamma}{}^{a}$	$I^{(rel.)}\gamma^b$	$E_i{}^c$	$a_2$	$a_4$	$J_i^\pi$	$\rightarrow$	$J_f^\pi$
(keV)		(keV)					
400.2	53(4)	8977	-0.244(31)	0.011(50)	$41/2^{-}$	$\rightarrow$	$39/2^{-}$
413.2	289(22)	1414	-0.101(62)	0.117(88)	$13/2^{+}$	$\rightarrow$	$11/2^{+}$
426.3	59(6)	4526	-0.484(51)	-0.004(74)	$25/2^{-}$	$\rightarrow$	$23/2^{-}$
438.2	1000(60)	1852	0.071(31)	0.068(45)	$17/2^{+}$	$\rightarrow$	$13/2^{+}$
443.6	62(5)	5654	-0.383(29)	0.154(43)	$31/2^{-}$	$\rightarrow$	$29/2^{-}$
454.4	33(3)	5340	-0.218(40)	0.076(59)	$29/2^{-}$	$\rightarrow$	$27/2^{-}$
460.5	63(4)	7444	-0.206(2)	0.056(2)	$35/2^{-}$	$\rightarrow$	$33/2^{-}$
469.6	48(6)	3749	-0.094(38)	0.030(55)	$21/2^{-}$	$\rightarrow$	$19/2^{-}$
488.2	75(6)	5207	-0.204(38)	-0.025(56)	$29/2^{-}$	$\rightarrow$	$27/2^{-}$
503.4	167(10)	6066	-0.237(52)	-0.053(78)	$33/2^{-}$	$\rightarrow$	$31/2^{-}$
509.3	69(6)	4719	-0.238(41)	0.140(60)	$27/2^{-}$	$\rightarrow$	$25/2^{-}$
514.3	75(8)	5779	0.276(59)	-0.109(87)	(27/2)	$\rightarrow$	(23/2)
532.1	276(18)	5180	-0.180(1)	0.039(2)	$29/2^{-}$	$\rightarrow$	$27/2^{-}$
537.7	54(4)	7982	-0.286(34)	0.188(50)	$37/2^{-}$	$\rightarrow$	$35/2^{-}$
550.1	58(5)	5890	-0.242(33)	0.138(48)	$31/2^{-}$	$\rightarrow$	$29/2^{-}$
551.1	31(4)	3439			$21/2^{-}$	$\rightarrow$	$19/2^{-}$
593.8	5(3)	4333			21/2	$\rightarrow$	23/2
595.5	56(4)	8577	-0.325(14)	0.025(21)	$39/2^{-}$	$\rightarrow$	$37/2^{-}$
611.3	463(28)	4648	-0.131(31)	-0.017(45)	$27/2^{-}$	$\rightarrow$	$25/2^{-}$
644.5	87(8)	4745	-0.187(24)	-0.063(35)	$25/2^-$	$\rightarrow$	$23/2^{-}$
659.0	90(8)	6439	0.278(36)	-0.126(53)	(31/2)	$\rightarrow$	(27/2)
659.7	83(10)	4100			$23/2^{-}$	$\rightarrow$	$21/2^{-}$
663.2	89(8)	5311	-0.225(35)	0.048(55)	$29/2^{-}$	$\rightarrow$	$27/2^{-}$
676.6	52(5)	4886	-0.03(10)	0.11(16)	$27/2^{-}$	$\rightarrow$	$25/2^{-}$
700.4	73(6)	6766	-0.291(60)	-0.067(93)	$35/2^{-}$	$\rightarrow$	$33/2^{-}$
741.5	45(4)	3534	0.243(61)	-0.155(93)	$21/2^{-}$	$\rightarrow$	$21/2^{+}$

TABLE I: Gamma rays assigned to  $^{107}\mathrm{In}$ 

$E_{\gamma}{}^{a}$	$I^{(rel.)}\gamma^b$	$E_i{}^c$	$a_2$	$a_4$	$J_i^\pi$	$\rightarrow$	$J_f^\pi$
(keV)		(keV)					·
791.0	419(28)	2793	-0.122(31)	0.023(52)	$21/2^{+}$	$\rightarrow$	19/2+
823.1	81(10)	7262	0.242(17)	-0.124(68)	(35/2)	$\rightarrow$	(31/2)
838.8	45(4)	7605	-0.179(34)	0.040(52)	$37/2^{-}$	$\rightarrow$	$35/2^{-}$
850.6	133(10)	3643	-0.296(4)	0.038(6)	$23/2^{-}$	$\rightarrow$	$21/2^{+}$
932.4	58(12)	5265			(23/2)	$\rightarrow$	21/2
934.0	75(12)	8196	0.253(54)	-0.183(81)	(39/2)	$\rightarrow$	(35/2)
945.8	57(8)	3739	-0.16(11)	0.19(16)	23/2	$\rightarrow$	$21/2^{+}$
1000.4	234(18)	1001	-0.050(36)	-0.076(53)	$11/2^{+}$	$\rightarrow$	$9/2^{+}$
1032.8	66(14)	2887	0.16(10)	0.13(16)	$19/2^{-}$	$\rightarrow$	$17/2^{+}$
1042.8	43(6)	4782	0.148(81)	-0.13(13)	27/2	$\rightarrow$	23/2
1055.0	68(12)	9251	0.241(24)	-0.089(37)	(43/2)	$\rightarrow$	(39/2)
1143.8	35(5)	5180	0.248(57)	-0.038(85)	$29/2^{-}$	$\rightarrow$	$25/2^{-}$
1220.1	49(12)	10471	0.297(41)	-0.045(61)	(47/2)	$\rightarrow$	(43/2)
1278.0	45(5)	3280	0.327(39)	-0.067(55)	$19/2^{-}$	$\rightarrow$	$19/2^{+}$
1333.2	50(4)	6983	-0.319(29)	0.059(44)	$33/2^{-}$	$\rightarrow$	$31/2^{-}$
1389.0	30(8)	11860	0.263(29)	0.028(45)	(51/2)	$\rightarrow$	(47/2)
1414.0	690(60)	1414	0.047(29)	0.004(43)	$13/2^{+}$	$\rightarrow$	$9/2^{+}$
1428.1	199(18)	3280	-0.137(25)	0.084(38)	$19/2^{-}$	$\rightarrow$	$17/2^{+}$
1437.4	290(18)	3439	-0.207(22)	0.049(35)	$21/2^{-}$	$\rightarrow$	$19/2^{+}$
1527.0	18(4)	5265			(23/2)	$\rightarrow$	23/2
1532.3	172(14)	3534	-0.337(10)	-0.036(15)	$21/2^{-}$	$\rightarrow$	$19/2^{+}$
1573.3	20(2)	13434	0.29(17)	-0.06(27)	(55/2)	$\rightarrow$	(51/2)
1746.5	48(6)	3749	-0.322(67)	0.026(96)	$21/2^{-}$	$\rightarrow$	$19/2^{+}$
1789.4	9(2)	15223			(59/2)	$\rightarrow$	(55/2)
1969.7	3(1)	17193			(63/2)	$\rightarrow$	(59/2)
2330.5	17(2)	4333	0.23(9)	0.24(13)	21/2	$\rightarrow$	19/2+

TABLE I: Gamma rays assigned to  $^{107}$ In

$E_{\gamma}{}^{a}$	$I^{(rel.)}\gamma^b$	$E_i{}^c$	$a_2$	$a_4$	$J_i^\pi$	$\rightarrow$	$J_f^\pi$
(keV)		(keV)					

<sup>&</sup>lt;sup>a</sup>Transition energies accurate to within  $\pm 0.5 \,\mathrm{keV}$ .

<sup>&</sup>lt;sup>c</sup>Excitation energies of initial states of  $\gamma$  transitions.

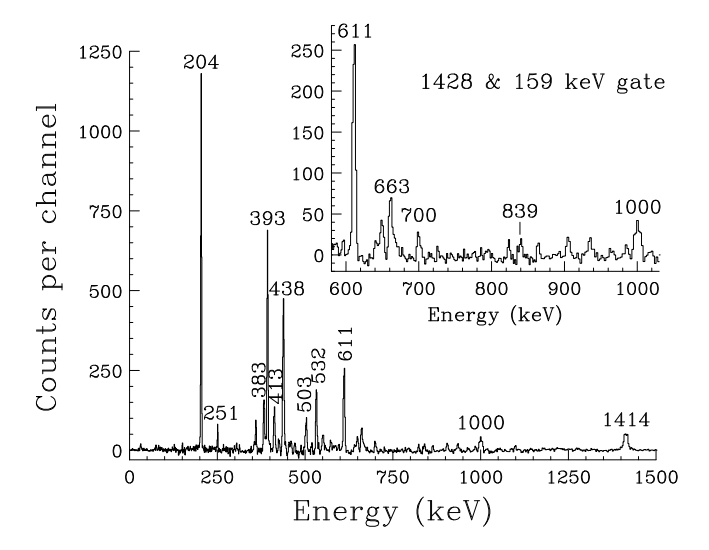


FIG. 3: Gamma-ray energy spectrum gated by the 1428 and 159 keV transitions. The inset enlarges the region between 600 keV and 1 MeV.

Above the isomeric  $19/2^+$  level, high-energy  $\gamma$ -ray transitions of  $\sim 1.5$  MeV connect to the  $19/2^-$  level at 3.280 MeV and  $21/2^-$  level at 3.534 MeV. These levels are suggested to be based on the  $\pi g_{9/2}^{-1} \otimes \nu(h_{11/2}, g_{7/2})$  configuration, i.e. a neutron excitation between the  $g_{7/2}$  and  $h_{11/2}$  sub-shells. The two sequences of magnetic dipole transitions have previously been observed to connect negative parity states up to  $33/2^{(-)}$  [8].

Gamma-ray coincidence relations of previously reported transitions [8] were confirmed as shown in the right part of partial level scheme in Fig. 2. Table I summarizes  $\gamma$  rays assigned to  $^{107}$ In. The relative intensity of each  $\gamma$  transition was extracted by fitting the  $\gamma$ - $\gamma$  correlation matrix by taking into account the  $\gamma$ -ray intensities of feeding transitions, branching ratio, and conversion coefficient of the lower transitions using the ESCL8R program in the RADWARE

<sup>&</sup>lt;sup>b</sup>Intensities are normalized to 1000 for the 438 keV  $\gamma$  transition.

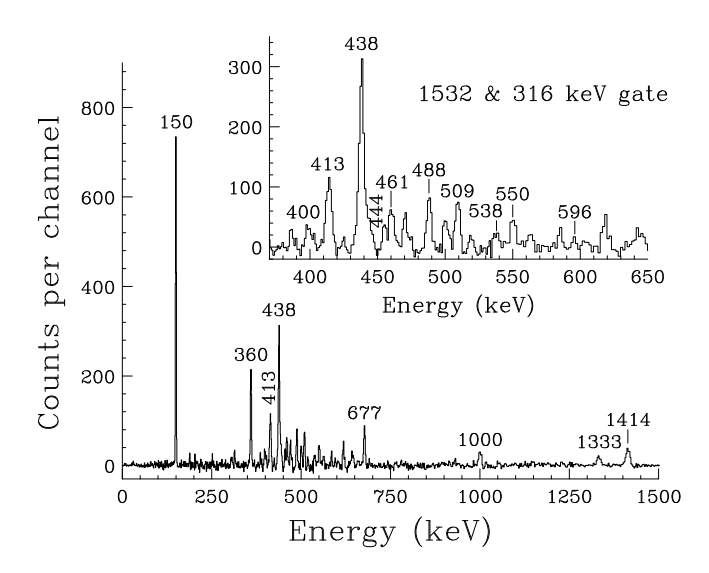


FIG. 4: Gamma-ray energy spectrum gated by the 1532 and 316 keV transitions. The inset enlarges the region between 350 and 650 keV.

software package [16].

By gating on the  $E_{\gamma}$ - $E_{\gamma}$  matrix and the  $E_{\gamma}$ - $E_{\gamma}$ - $E_{\gamma}$  cube, coincidence relations between known  $\gamma$  rays and newly observed  $\gamma$  rays were examined. Fig. 3 shows a  $\gamma$  ray energy spectrum obtained by double gating in the cube on the 1428 and 159 keV transitions which are members of one of the sequences of magnetic dipole transitions (M1-band 1). Gammaray transitions up to the  $33/2^-$  level at 6.066 MeV (see Fig. 2) were confirmed and two new transitions, 700 and 839 keV, were placed above this level. These two transitions also have M1 character as shown in table I.

Fig. 4 shows a spectrum obtained by double-gating in the cube on the 1532 and 316 keV transitions which are members of another M1 sequence (M1-band 2). Gamma-ray transitions up to the  $33/2^-$  level at 6.983 MeV were confirmed and in addition four  $\gamma$ -ray transitions were observed in coincidence with the sequence. Based on the angular distribution analysis, the multipolarities of these four transitions were assigned as M1 and accordingly the spins and parities of the four levels above the  $33/2^-$  level were assigned up to the  $41/2^-$  level at 8.977 MeV.

In addition to the above mentioned M1 transitions, a rotational  $\gamma$ -ray cascade (STB1) consisting of the 514, 659, 823, 934, 1055, 1220, 1389, 1573, and 1789 keV transitions was observed by gating on the  $E_{\gamma}$ - $E_{\gamma}$  matrix as shown in Fig. 2 and 5. A 1970 keV transition was tentatively placed on top of the band. The 934 keV transition has a larger intensity

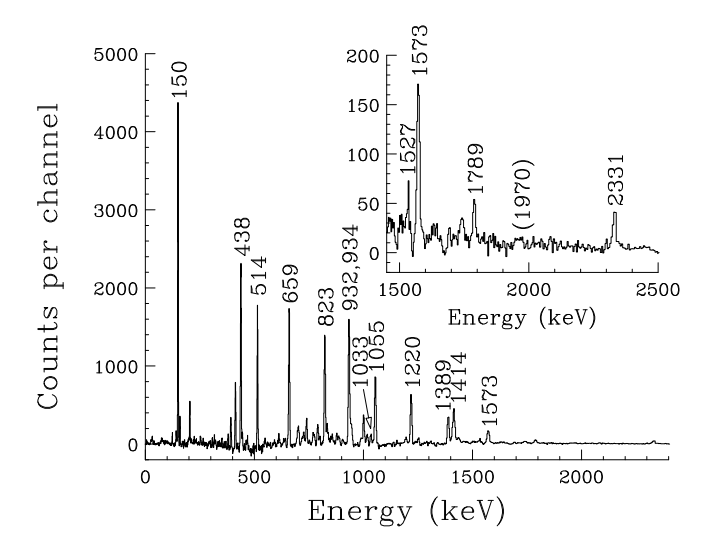


FIG. 5: Sum of  $\gamma$ -ray energy spectra created by double-gating on the in-band transitions of the rotational band (STB1). The inset enlarges the region between 1.45 and 2.5 MeV.

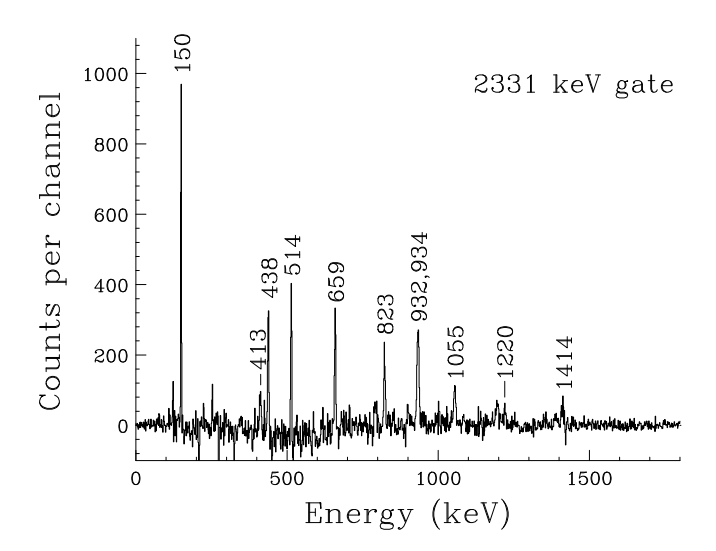


FIG. 6: Gamma-ray energy spectrum gated by the 2331 keV linking transition from the  $\gamma - \gamma$  matrix.

than the other neighboring in-band transitions, 823 and 1055 keV since it is a self-coincident doublet decomposed of a 932 keV and a 934 keV transition. Based on the intensity balance of the in-band transitions, a rotational band structure was assigned as shown in the left part of Fig. 2. In addition, the 2331 keV  $\gamma$  ray is observed to be in coincidence with the assigned in-band transitions as well as the low-lying transitions, 150, 438, 413, and 1414 keV (see Fig. 6). Since this  $\gamma$  ray is strongly in coincidence with the lowest-lying member of the band, as well as with the 932 keV-934 keV doublet, the decay path of the band is formed

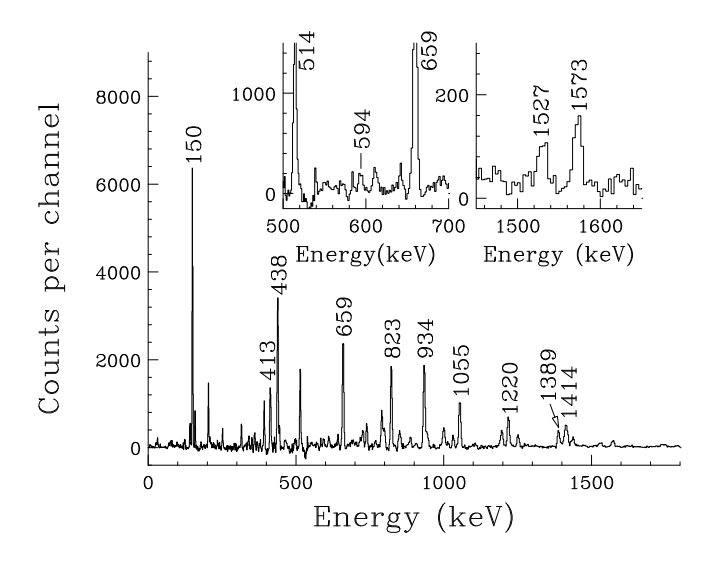


FIG. 7: Gamma-ray energy spectrum created by gating on the in-band transition of the rotational band in one axis, and the 946, 791, 150, 438, 413, 1000, and 1414 keV transitions in the other axis of  $\gamma\gamma\gamma$  cube. The insets enlarge the regions from 0.5 MeV to 0.7 MeV, and from 1.45 MeV to 1.65 MeV, respectively.

to precede the cascade of 932 and 2331 keV transitions to the  $19/2^+$  state at 2.002 MeV as shown in the level scheme. Note that the intensity of the 932 keV transition in Table I is larger than the sum of the 2331 keV and 594 keV intensities. Our interpretation is that there might be several weak unidentified  $\gamma$  transitions decaying from the 4.333 MeV level carrying the intensity not accounted for. For example, in the double-gated spectrum on the in-band transitions (Fig. 5), a peak appeared at 1033 keV. This indicates the presence of a linking transition from the 4.333 MeV level to the 2.887 MeV level. However, any such  $\gamma$  transitions were not observed due to the low statistics.

There is another decay path of the band via the 1527 keV transition from the 5.265 MeV state to the 3.739 MeV state. Fig. 7 shows a  $\gamma$ -ray energy spectrum created by gating on the in-band transitions of STB1 on one axis, and the 946, 791, 150, 438, 413, 1000, and 1414 keV transitions on the other axis of the  $\gamma\gamma\gamma$  cube. As shown in the figure, the 594 and 1527 keV transitions are coincident with the in-band transitions above 5.265 MeV level as well as transitions below 3.739 MeV level. These 594 and 1527 keV transitions correspond to the links from 4.333 to 3.739 MeV level and from 5.265 to 3.739 MeV level, respectively. These two decay paths establish the excitation energy of the observed lowest level of the band to be 5.265 MeV.

In Fig. 5, the 1573 keV peak appears stronger than the 1527 keV peak compared to the relative intensities presented in Table I. Since the spectrum shown in Fig. 5 was created by double-gating on the in-band transitions of STB1 including the 932, 934 keV doublet, it contains double-gating between the 932 keV  $\gamma$  ray and other  $\gamma$  rays of STB1. Therefore, the counts in the 1573 keV peak in Fig. 5 was artificially increased relative to that of the 1527 keV transition.

The excitation energies of the yrast levels and the levels in the STB1 were plotted as a function of spin in the upper panel of Fig. 8. In the lower panel of Fig. 8, relative intensities of the yrast transitions and the in-band transitions are plotted. One can see that the M1-band 1 becomes yrast above spin 10  $\hbar$ , and that the STB1 becomes yrast around spin 18  $\hbar$ . The intensity profiles are consistent with the trend of yrast sequences formed by M1-band 1 and STB1.

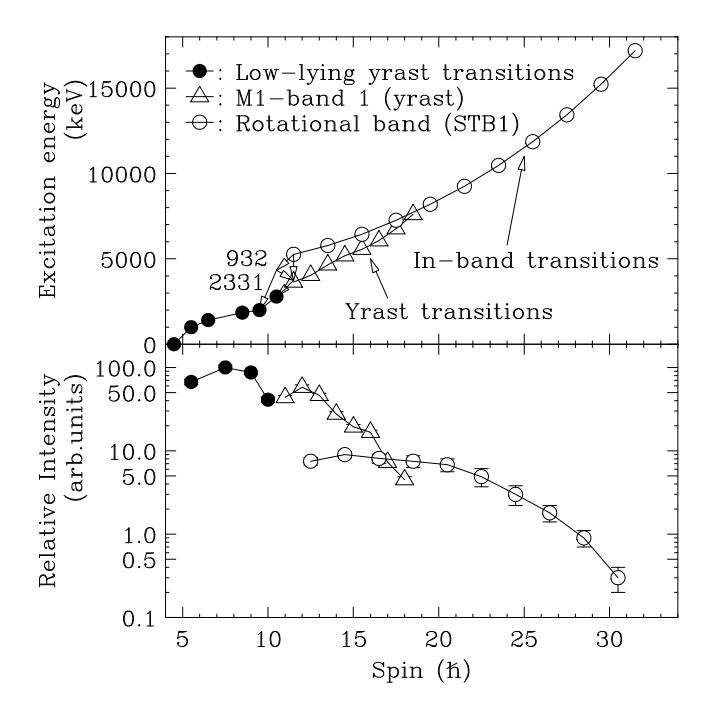


FIG. 8: Excitation energies of the yrast levels and the levels in the rotational band as a function of spin (upper panel). Relative intensities of yrast  $\gamma$  transitions and those of the band are plotted as a function of spin in the lower panel.

Multipolarity assignments for the observed  $\gamma$ -ray transitions were deduced from the angular distribution analysis. Fig. 9 displays the  $a_2$  and  $a_4$  coefficients of the  $\gamma$ -ray angular distribution function plotted as a function of the  $\gamma$ -ray energy. Filled circles and filled

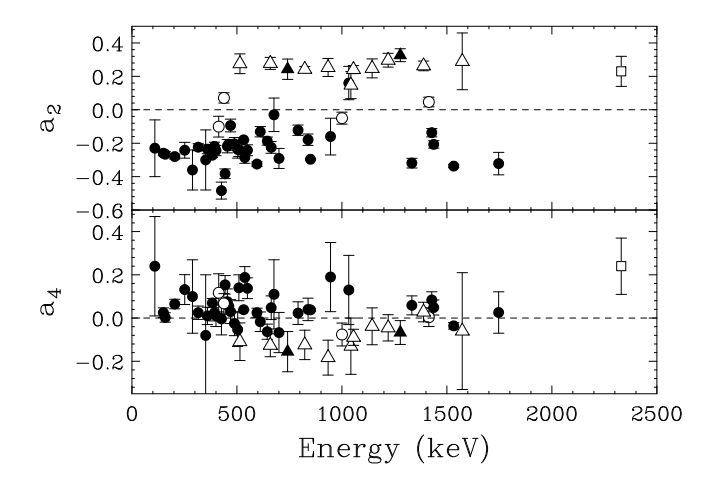


FIG. of  $a_2$ and  $a_4$ coefficients of angular distributions,  $W(\theta)=a_0(1+a_2P_2(\cos\theta)+a_4P_4(\cos\theta))$ , as a function of  $\gamma$ -ray energy. Here,  $\theta$  is the emission angle of  $\gamma$  rays relative to the beam axis and  $P_n(\cos\theta)$  are the Legendre polynomials. Filled circles and filled triangles correspond to the angular distribution of known M1 and  $\Delta I=0$  E1 transitions, respectively. Open circles indicate those of the transitions below the isomeric state at 1.852 MeV. Open triangles correspond to those of the identified in-band transitions as well as known E2 transition (1144 keV). The open square is for the case of the 2331 keV linking transition.

triangles correspond to the angular distribution of known M1 transitions and  $\Delta I=0$  E1 transitions, respectively, which agree with theoretical estimates. Open circles are for the  $\gamma$ -ray transitions decaying from the isomeric state at 1.852 MeV and they show small values as expected. Open triangles correspond to those of the newly identified cascade transitions which are consistent with a stretched E2 character.

As shown in Fig. 9, the angular distribution of the 2331 keV linking transition (open square) does not clearly determine its multipolarity due to the low statistics. The positive  $a_2$  value may indicate that it contains a quadrupole component in its multipolarity and the positive  $a_4$  may reflect a mixed transition. In order to try and resolve this ambiguity, the mixing ratio that satisfies the 99.9% confidence limit test in  $\chi^2$  (defined as in equation (1) [18]) is plotted as a function of  $\tan^{-1}\delta$  in Fig. 10. Three different hypotheses were tested,  $19/2\rightarrow 19/2$ ,  $21/2\rightarrow 19/2$ , and  $23/2\rightarrow 19/2$ .

$$\chi^2 = \frac{[a_2 - a_2(cal)]^2}{3(\Delta a_2)^2} + \frac{[a_4 - a_4(cal)]^2}{3(\Delta a_4)^2}$$
 (1)

As indicated in Fig. 10, a parameter ' $\sigma/J$ ' is used to implement the initial alignment, where

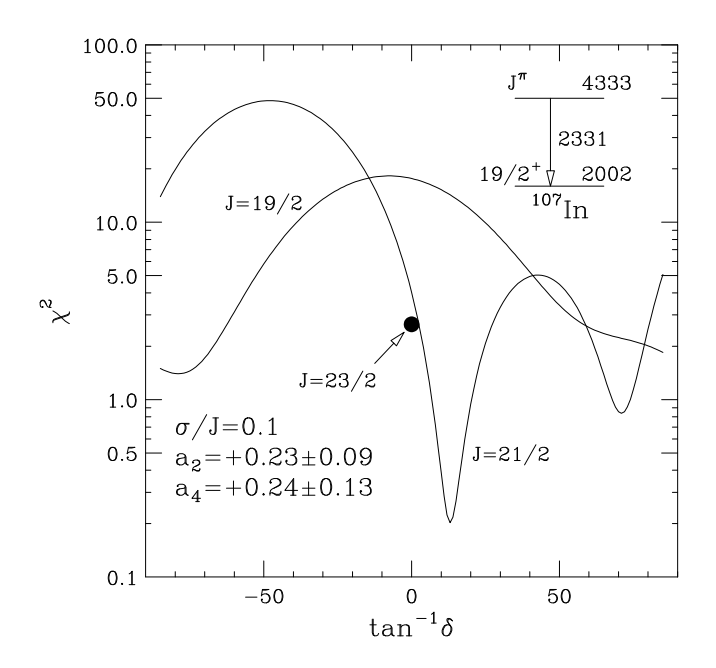


FIG. 10:  $\chi^2$  vs tan<sup>-1</sup> $\delta$  curves for the 2331 keV transition in <sup>107</sup>In. The parameters indicated were used to compute the curves.

a Gaussian distribution for the magnetic substates is assumed and  $\sigma$  and J denote the width and the spin, respectively. In the calculation, a ratio  $\sigma/J=0.1$  was assumed. The  $\chi^2$  result suggests a mixed E2/M1 or M2/E1 transition,  $21/2\rightarrow19/2^+$  with a mixing ratio of 0.23. Since Weisskopf estimate of lifetimes for a 2331 keV  $\gamma$  ray are 0.4 ps for an E2 and 29 ps for an M2 transition, respectively, both cases are short enough for prompt  $\gamma$  coincidence and therefore the parity of the 4.333 MeV state was not determined. Since the decay-out 932 keV  $\gamma$ -ray transition in cascade with the linking transition is close in energy to the 934 keV in-band transition, its multipolarity was not firmly identified. The statistics of another 1527 keV linking transition were too low to perform angular distribution analysis in order to establish the multipolarity. Under the assumption that a dipole transition connects the lowest level of the band with the 4.333 MeV level, the spin of the band was assigned as starting with (23/2) as shown in Fig. 2.

#### IV. DISCUSSION

In this mass region, the presence of rotational bands has been reported previously in the N=58 isotones, <sup>105</sup>Ag, <sup>106</sup>Cd, <sup>108</sup>Sn, <sup>109</sup>Sb, <sup>110</sup>Te, and <sup>111</sup>I [3, 6, 7, 19–23]. Among them,

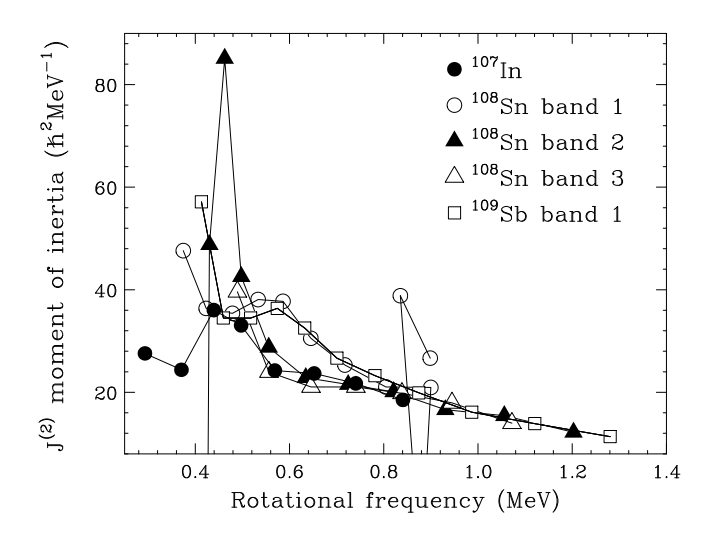


FIG. 11: Experimentally deduced dynamical moments of inertia  $J^{(2)}$  in  $^{107}$ In,  $^{108}$ Sn, and  $^{109}$ Sb. The data on  $^{107}$ In is from the present work.

rotational bands exhibiting a character of smooth band termination appeared only in  $^{108}$ Sn,  $^{109}$ Sb, and  $^{110}$ Te.

In Fig. 11, deduced dynamical moments of inertia  $J^{(2)}$  are shown as a function of rotational frequency. Here, the rotational frequency ( $\omega$ ) and the dynamical moment of inertia  $J^{(2)}$  are deduced from the experimental data ( $E_{\gamma}$ ) using the formulae,

$$\hbar\omega = \frac{dE}{dI} \approx \frac{E_{\gamma}}{2} \tag{2}$$

and

$$J^{(2)} = \frac{dI}{d\omega} \approx \frac{4}{\Delta E_{\alpha}},\tag{3}$$

respectively. In addition to the band in  $^{107}$ In, also the bands in  $^{108}$ Sn [6], and  $^{109}$ Sb [22] are shown, which have positive parity for the neutron configuration according to the assignments based on the cranked Nilsson-Strutinsky calculations [24]. In general, all  $J^{(2)}$  values show the smooth decrease with increasing rotational frequency which is characteristic for smooth band termination in systems with weak pairing [4, 24]. This feature is disturbed only at the top of the band 1 in  $^{108}$ Sn. The  $J^{(2)}$  values of  $^{107}$ In show very close similarity with those in bands 2 and 3 of  $^{108}$ Sn, while those in band 1 of  $^{108}$ Sn and band 1 of  $^{109}$ Sb are also very similar. This suggests that the structure of the band in  $^{107}$ In is similar to that of bands 2 and 3 in  $^{108}$ Sn. Bands 2 and 3 of  $^{108}$ Sn were interpreted to be signature partner bands with the proton configuration of  $\pi[g_{9/2}^{-2} \otimes (g_{7/2}h_{11/2})]$  [6, 25]. On the other hand, band 1 of  $^{108}$ Sn and  $^{109}$ Sb

were understood to have configurations of  $\pi[g_{9/2}^{-2}\otimes g_{7/2}^2]$  and  $\pi[g_{9/2}^{-2}\otimes g_{7/2}^2h_{11/2}]$ , respectively. The hump observed in the  $J^{(2)}$  plot for band 1 of  $^{108}\mathrm{Sn}$  and  $^{109}\mathrm{Sb}$ , appearing at  $\sim 0.55$  MeV, was interpreted as due to the alignment of  $g_{7/2}$  protons based on cranked Woods-Saxon calculations [25]. These results indicate that deformation-driving down-sloping  $\pi g_{7/2}$  and  $\pi h_{11/2}$  orbitals and, especially, the holes in the  $\pi g_{9/2}$  extruder orbitals play an important role to create the rotational band structures which undergo smooth band termination in this mass region [24]. In the case of  $^{107}\mathrm{In}$ , possible configurations of the observed band (STB1) would be  $\pi[g_{9/2}^{-2}\otimes g_{7/2}]$  or  $\pi[g_{9/2}^{-2}\otimes h_{11/2}]$  generated by removing one proton from  $^{108}\mathrm{Sn}$ .

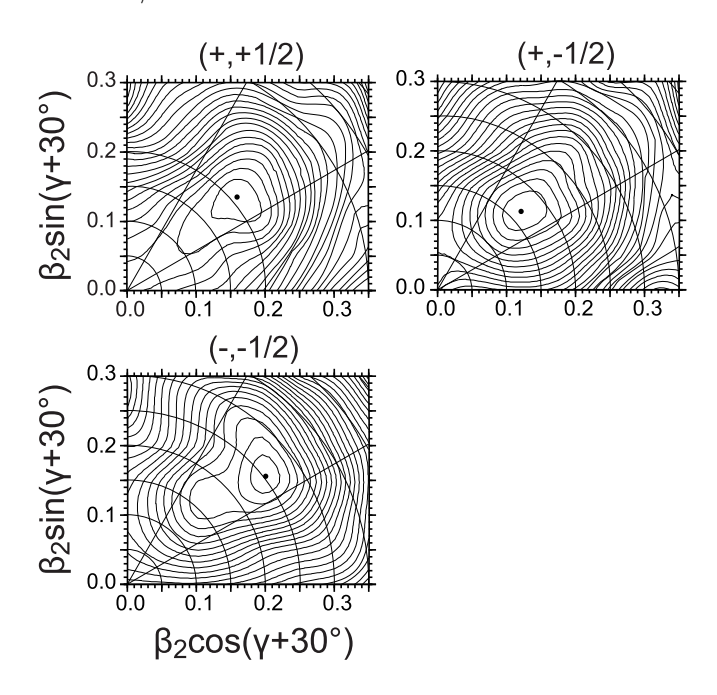


FIG. 12: Calculated total Routhian surfaces (TRS) at a rotational frequency of 0.75 MeV. The lowest positive-parity configurations with signature +1/2 and -1/2 are shown in the left and right upper panels, respectively, while the lowest negative-parity configuration with signature -1/2 is plotted on the lower left panel.

Cranked Strutinsky calculations based on the Woods-Saxon (WS) [26] and Nilsson (CNS) [4, 24] potentials were performed in order to interpret the structure of the observed rotational band (STB1). In the former total Routhian Surface (TRS) calculations, pairing correlations were taken into account by means of a seniority and double stretched quadrupole pairing force [27]. Approximate particle number projection was performed via the Lipkin-Nogami method [28, 29]. Each quasiparticle configuration was blocked self-consistently. The energy in the rotating frame of reference was minimized with respect to the deformation parameters

 $\beta_2, \beta_4$  and  $\gamma$ . Deformed minima in the total Routhian surfaces (TRS) were found at  $(\beta_2, \gamma) \sim (0.20, 10^{\circ})$  for both signatures at positive parity  $(\pi, \alpha) = (+, \pm 1/2)$  and at  $(\beta_2, \gamma) \sim (0.25, 8^{\circ})$  for the negative parity, negative signature configuration (-, -1/2) as shown in Fig. 12. The structure of the experimentally observed rotational band (STB1) in <sup>107</sup>In is likely to correspond to one of these configurations.

Excitation energies, kinematic ( $J^{(1)}$ ) and dynamic ( $J^{(2)}$ ) moments of inertia obtained from the TRS calculations are compared with experimental values in Fig. 13. In order to deduce the experimental  $J^{(1)}$ -moment of inertia, we have assumed the spin of the lowest level of the band to be 23/2. The TRS calculation shows that the configuration of positive parity with negative signature (+, -1/2) is lowest in energy among the predicted configurations in the frequency range of interest. However, as can be seen in Fig. 13,  $J^{(1)}$  and  $J^{(2)}$  moments of inertia for  $(+, \pm 1/2)$  configurations show quite different behavior comparing with the experimental values. On the other hand, the configuration with (-, -1/2) is in better agreement with the experimental properties except for the high frequency region. However, it is quite likely that the TRS calculations overestimate the role of pairing at high spin and this leads to observed discrepancies between experiment and calculations.

In the CNS [4, 24] calculations, the pairing is neglected and thus the results are expected to be realistic only at high spin,  $I \ge 15\hbar$ . In general, a very good agreement [4] between the CNS calculations and observed high-spin bands in this mass region has been obtained with the  $\kappa$ - and  $\mu$ -values from Ref. [30] and these are the values which are used also in the present study. The calculations in the current analysis are performed using the CNS version of Ref. [31], so that not only the relative energies between the bands but also the absolute energy scale can be compared. The single-particle configurations are defined by the occupation of low- and high-j orbitals. The total energy of each configuration is minimized at each spin in the  $(\varepsilon_2, \varepsilon_4, \gamma)$  deformation plane. Standard CNS labeling of each configuration is used. This shorthand notation is based on the number of particles in different j shells for each configuration. The j shells are pure only if the shape is spherical. Thus, in general the labeling refers to the dominant shell only, while the wave functions also contain components from other N and j shells. Relative to a closed <sup>100</sup>Sn core, a shorthand configuration label

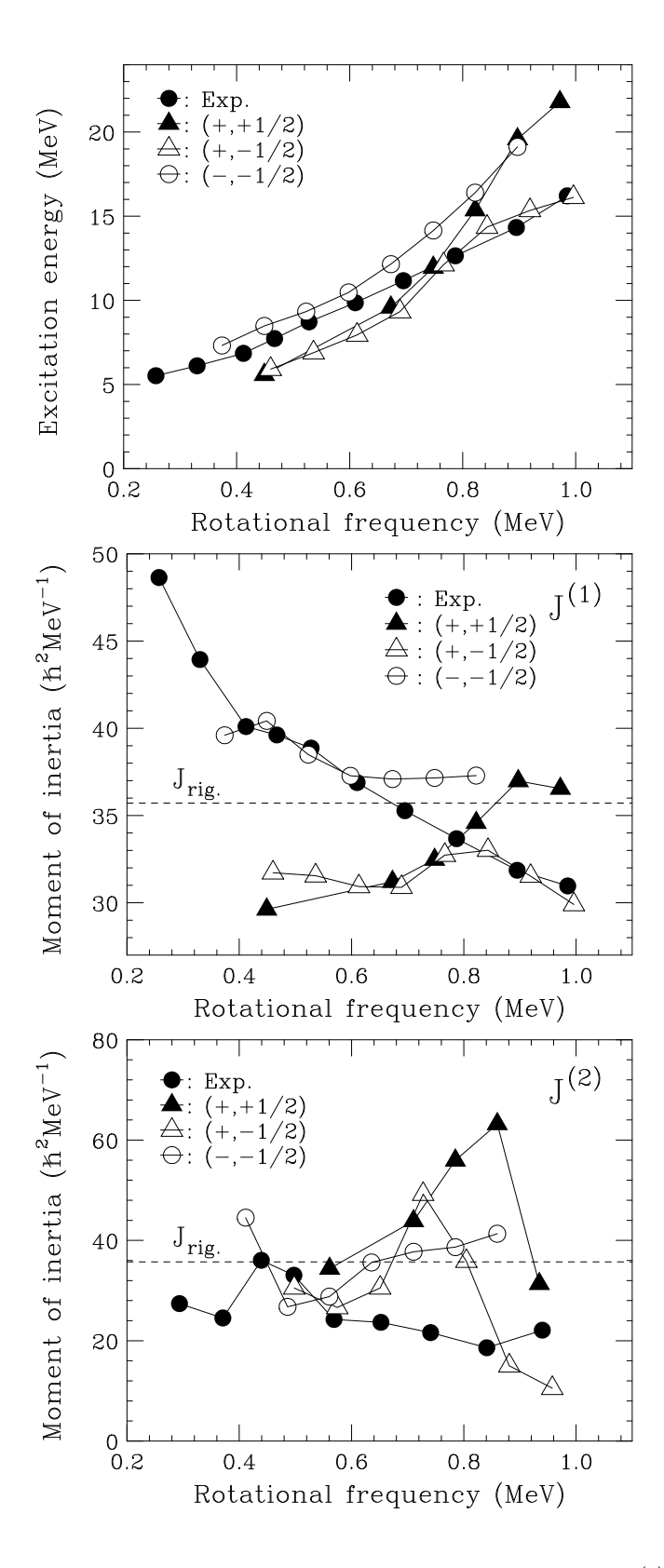


FIG. 13: Comparison of experimental and calculated excitation energies,  $J^{(1)}$  and  $J^{(2)}$  moments of inertia as a function of rotational frequency. The highest-frequency data point, which is originated from the tentatively assigned 1970 keV transition, is also included in the plot. Theoretical values were obtained by TRS calculations. The dashed line marks the rigid-body moment of inertia for a deformation parameter  $\beta_2 = 0.25$ .

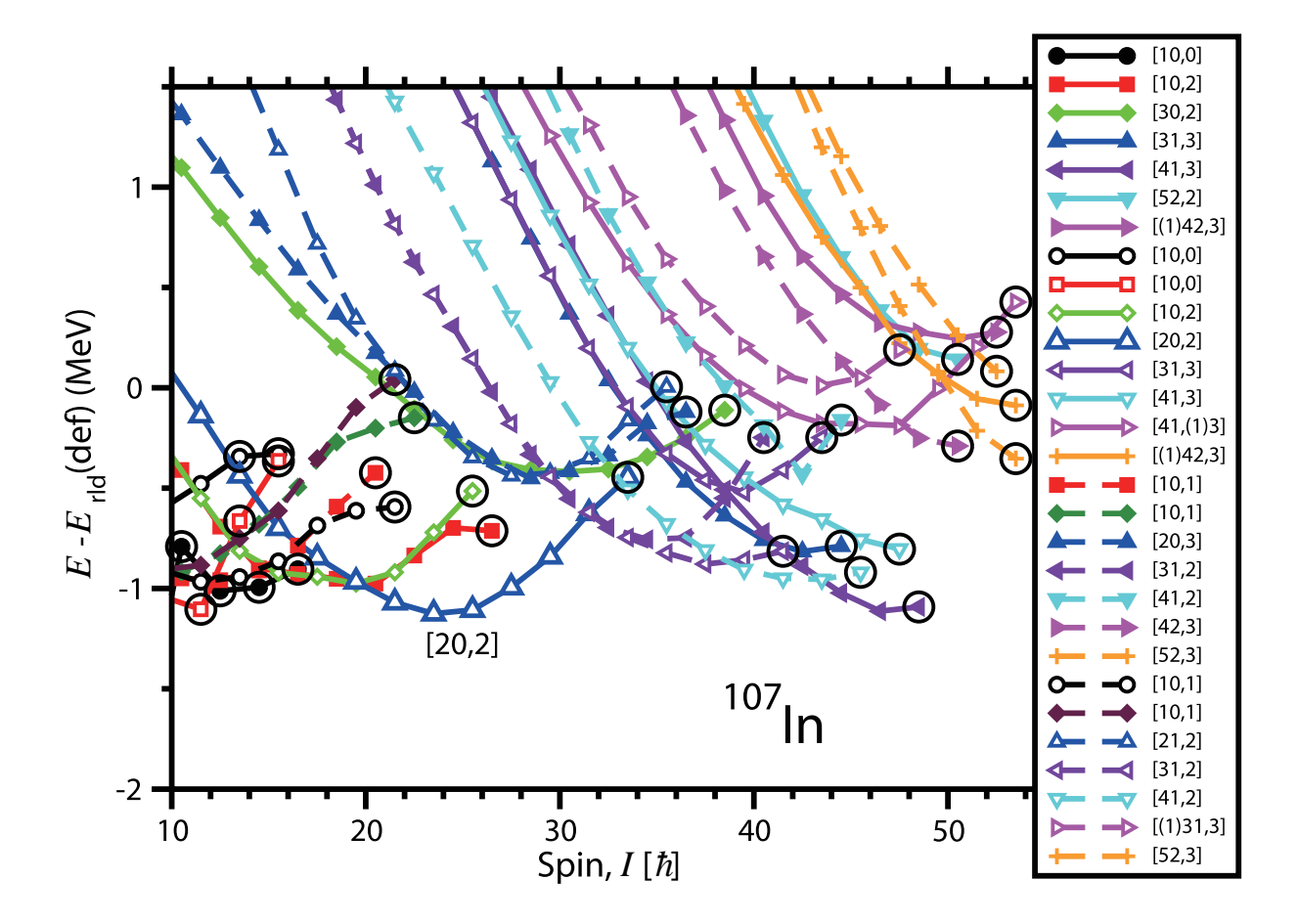


FIG. 14: (Color online) Calculated energies of the configurations forming the yrast line in four combinations of parity and signature shown relative to rigid rotor reference. Large open circles indicate terminating and aligned states. Solid and dashed lines are used for positive and negative parity states, respectively. Solid and open symbols are used for the signatures  $\alpha = +1/2$  and  $\alpha = -1/2$ , respectively. Configuration labels are shown in the legend.

 $[(p_1)p_2p_3, (n_1)n_2]$  can be written as [4]

$$[(p_1)p_2p_3, (n_1)n_2] = \pi(N=3)^{-p_1}(g_{9/2})^{p_2}(h_{11/2})^{p_3}$$

$$\otimes \nu(N=3)^{-n_1}(h_{11/2})^{n_2}$$
(4)

with the remaining particles (protons/neutrons) outside the core located in the mixed  $(d_{5/2} g_{7/2})$  orbitals. The label  $p_1$   $(n_1)$  is dropped if no holes are generated in the N=3 proton (neutron) shell.

The results of the calculations are shown in Fig. 14. One can see that the [20,2] configuration dominates the yrast line in the spin range  $I = 20 - 31\hbar$ . This configuration is

therefore the most likely counterpart for the observed decoupled  $\Delta I = 2$  band. Fig. 15 compares the experimental band with the results of the calculations. Fig. 15a shows the experimental band for three different spin assignments  $I_0$  for the lowest state in the band. Fig. 15b displays the configurations which can be possible counterparts of the experimental band. In Fig. 15a,b, the y axis denotes the energy with the rotating liquid drop (rld) energy [31] subtracted. The energy difference between the predictions and observations is plotted in Fig. 15c. In the ideal case when the transition energies will be predicted correctly by the calculations for each transition in the band, the curve of the band in Fig. 15c will have a constant energy difference for all states of a given configuration, i.e. it will be horizontal. Furthermore, if the absolute energy is predicted correctly, this difference should be zero with the experience [31] that the difference will generally be smaller than one MeV, i.e. the absolute energy at high spin can be described with a similar accuracy as ground state masses. One can see that reasonable agreement between theory and experiment is obtained when the [20,2] configuration is assigned to the band; the deviation from the horizontal line in Fig. 15c of  $\sim 1$  MeV is at the upper limit of the typical discrepancies between theory and experiment. For this configuration assignment, the observed band in <sup>107</sup>In is one transition short of termination. Further support for this configuration assignment comes from the analysis of the configurations of the smooth terminating bands in the N=58 isotones (see Fig. 23 in Ref. [4]). In  $^{108}$ Sn, the yrast line in the spin range  $I=20-28\hbar$  is dominated by the [20,2] configuration. This is exactly the same configuration (in terms of shorthand notation) as we assign to the  $\Delta I = 2$  band in <sup>107</sup>In. The difference between the [20,2] configurations in these two nuclei is related to an occupation of the extra  $(d_{5/2} g_{7/2})$  proton in <sup>108</sup>Sn. Note also that this configuration assignment fits exactly into the systematics of the configurations of smooth terminating bands observed in this mass region (see Fig. 20 and 23 in Ref. [4]). Indeed, according to this figure, the present signature  $\alpha = -1/2$  [20,2] band is predicted to be the most favored smooth terminating band in <sup>107</sup>In.

The evolution of the potential energy surfaces for the [20,2] configuration is shown in Fig. 16. This configuration displays typical features of smooth band termination gradually evolving from near-prolate shape at low spin up to a non-collective oblate shape at the terminating state with  $I^{\pi} = 67/2^{+}$ . These energy surfaces are very regular thus showing no disturbances, neither from mixing with aligned states within the same configuration (see Ref. [4] for more details of such mechanism) nor from mixing with other collective

configurations. This is a consequence of the fact that the nuclear system attempts to avoid a high level density in the vicinity of the Fermi level by a gradual adjustment of the equilibrium deformation with increasing spin [4].

Taking into account the uncertainty of spin-parity definition of the experimental  $\Delta I = 2$ band, one can consider also alternative configuration assignments. These are the [30,2], [20,3] and [21,2] configurations (Fig. 14). The [30,2] configuration involves an additional excitation from the proton  $g_{9/2}$  subshell, while the [20,3] ([21,2]) configurations are built from the [20,2] configuration by moving the neutron from  $(d_{5/2} g_{7/2})$  into  $h_{11/2}$  (by moving the proton from  $(d_{5/2} g_{7/2})$  into  $h_{11/2}$ ). These changes require additional energy, and thus these configurations are less energetically favored than [20,2] (Figs. 14 and 15b). In addition, the spin of the lowest state in the band has to be changed either to 21/2 or to 25/2 if either the [30,2] or [20,3] configurations is to be assigned to the experimental band. Note that the calculated energies for the [20,3] and [30,2] configurations are similar (Fig. 15b). Thus, the [20,3] configuration is not shown in Fig. 15c. The systematics of the configuration assignments for smoothly terminating bands in the N=58 isotones (Fig. 20 and 23 in Ref. [4]) also disfavors the assignment of these configurations. A '[21' proton configuration corresponds to  $\pi(g_{9/2})^{-2}(h_{11/2})^1$ , i.e. the first  $h_{11/2}$  orbital is filled before any positive parity orbital above Z = 50 is filled, which is clearly unexpected considering that the  $h_{11/2}$  shell is located substantially higher in energy than the  $g_{7/2}$  (and  $d_{5/2}$ ) subshell. Indeed, the configurations of this type become yrast in neighboring <sup>108</sup>Sn nucleus only above  $I \approx 28\hbar$ . Furthermore configurations of the type [30,2] with 3  $g_{9/2}$  proton holes have not been assigned to any smooth terminating band in this region while configurations with three  $g_{9/2}$  neutrons are only energetically favoured at higher spin values,  $I \approx 30 - 40$  (Ref. [4]).

One can see that it is only the [20,2] configuration which gives a reasonable description of the experimental data. Note that the energy difference between calculations and experiment for the [20,2] configuration (Fig. 15c) is similar to that for other terminating bands in this region, see Fig. 1 of Ref. [31], with a constant and somewhat negative value around 0.5-0.8 MeV in an extended spin range before termination. All the other curves show very different features. Thus, the CNS comparison with experiment clearly selects the [20,2] configuration as the only reasonable assignment for the observed band.

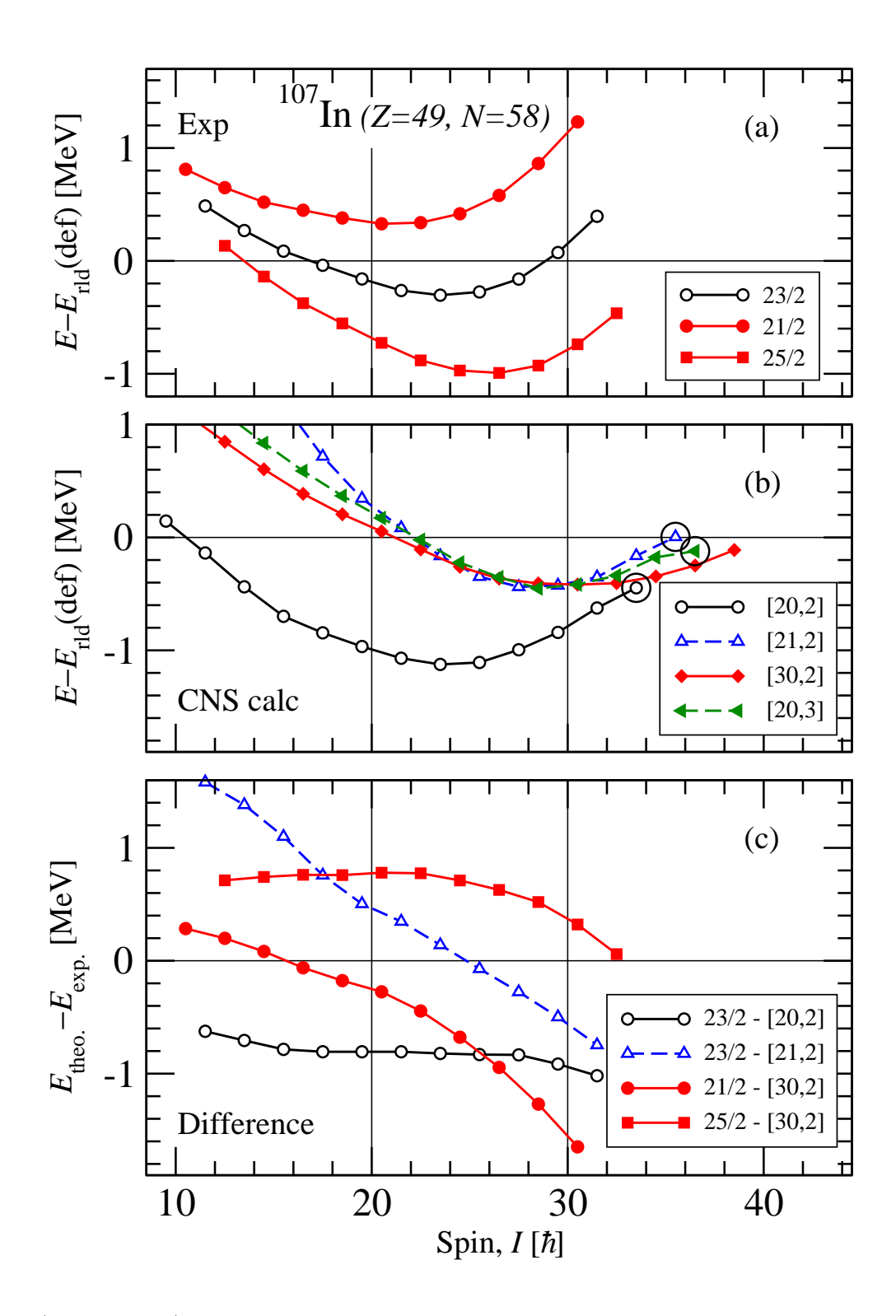


FIG. 15: (Color online) Comparison between the experimentally observed  $\Delta I = 2$  rotational band (STB1) and the CNS predictions for selected configurations. The top panel shows the experimental band with different spin assignments  $I_0$  for the lowest observed state. The middle panel shows the chosen predicted configurations. The bottom panel plots the energy difference between the predictions and observations.

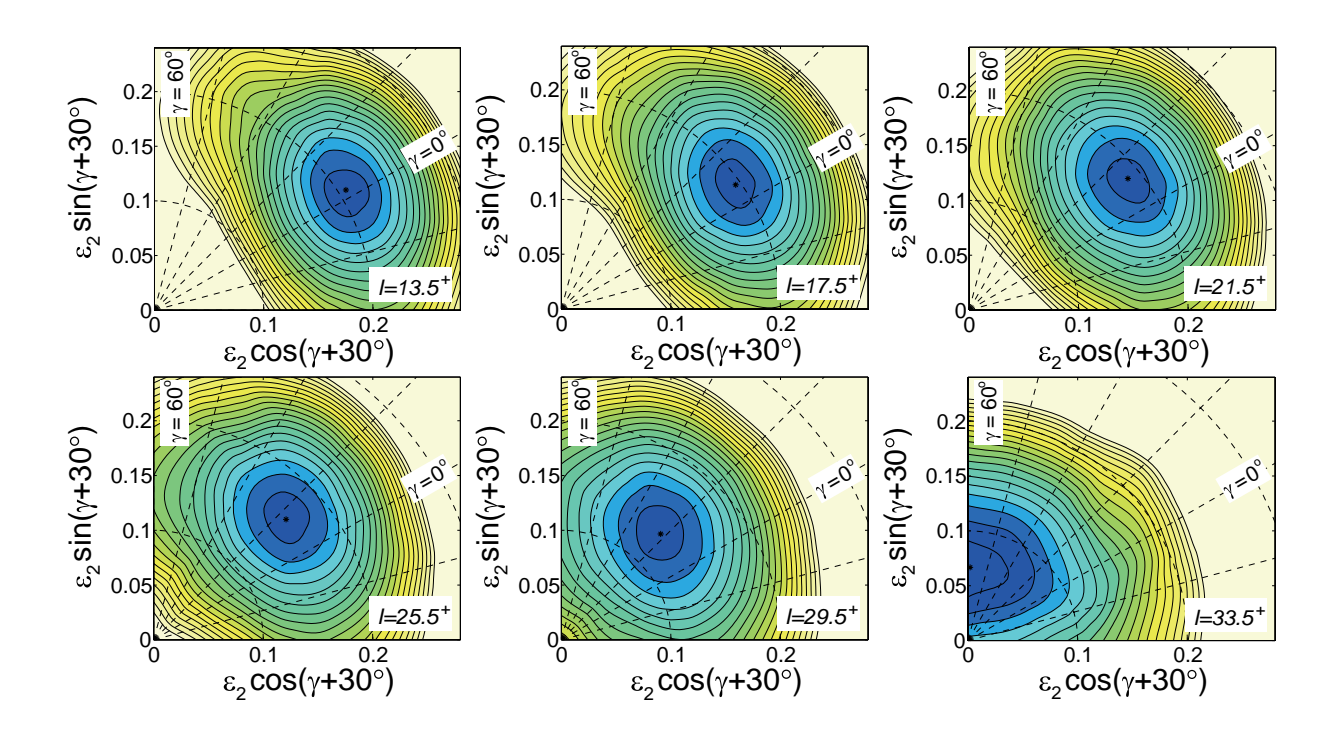


FIG. 16: (Color online) Evolution of the potential energy surfaces (PES) for the [20,2] configuration in  $^{107}$ In. The six PES figures are given in steps of  $4\hbar$  from the near-prolate state at  $I=13.5^+$  up to the terminating state at  $I=33.5^+$ . The energy difference between two neighboring equipotential lines is 0.2 MeV and the last equipotential line corresponds to 4.0 MeV excitation with respect to the minimum.

# V. SUMMARY

In summary, a rotational band structure with ten E2 cascade transitions has been observed in  $^{107}$ In. The J<sup>(1)</sup> and J<sup>(2)</sup> moments of the band exhibit a gradual decrease with increasing rotational frequency, a typical characteristic of the smoothly terminating bands in this mass region. The experimental results were compared with Total Routhian Surface (TRS) and Cranked Nilsson-Strutinsky (CNS) calculations. In the former case, pairing was taken into account and in the latter, it was neglected. In both calculations, the configuration with positive parity and negative signature (+, -1/2) was energetically most favored in the spin range  $I = 20 - 31\hbar$ . According to the CNS calculations, the observed band has a [20,2] structure: under this configuration assignment it is one transition short of termination. However, the TRS calculations give some preference for a negative parity assignment instead, corresponding to an approximate [21,2] configuration at high spin using the CNS labels. Further experimental investigations of this nucleus will be useful to observe higher

spin levels and definitely fix the spin of the observed band.

## Acknowledgments

The authors would like to thank Geirr Sletten and Jette Sørensen at NBI, Denmark for preparing the targets. We thank the UK/France (STFC/IN2P3) Loan Pool and GAMMAPOOL European Spectroscopy Resource for the loan of the detectors for JUROGAM. This work was supported by the Swedish Research Council, the Academy of Finland under the Finnish Center of Excellence Programme 2000–2005 (Project No. 44875, Nuclear and Condensed Matter Physics Programme at JYFL), UK STFC, the Göran Gustafsson foundation, the JSPS Core-to-Core Program, International Research Network for Exotic Femto System, the European Union Fifth Framework Programme "Improving Human Potential—Access to Research Infrastructure" (Contract No. HPRI-CT-1999-00044), by the U.S. Department of Energy under Grant DE-FG02-07ER41459, and was also supported by a travel grant to JUSTIPEN (Japan-US Theory Institute for Physics with Exotic Nuclei) under U.S. Department of Energy Grant DE-FG02-06ER41407.

<sup>[1]</sup> A. Gadea *et al.*, Phys. Rev. C **55**, R1 (1997).

<sup>[2]</sup> I. Ragnarsson, V.P. Janzen, D.B. Fossan, N.C. Schmeing, and R. Wadsworth, Phys. Rev. Lett. 74, 3935 (1995).

<sup>[3]</sup> V.P. Janzen *et al.*, Phys. Rev. Lett., **72**, 1160 (1994).

<sup>[4]</sup> A. V. Afanasjev, D. B. Fossan, G. J. Lane and I. Ragnarsson, Phys. Rep. 322, 1 (1999).

<sup>[5]</sup> A. O. Evans et al., Phys. Lett. **B636**, 25 (2006).

<sup>[6]</sup> R. Wadsworth et al., Phys. Rev. C 53, 2763 (1996).

<sup>[7]</sup> E. S. Paul *et al.*, Phys. Rev. **C76**, 034323 (2007).

<sup>[8]</sup> S.K. Tandel et al., Phys. Rev. C 58, 3738 (1998).

<sup>[9]</sup> S. Sihotra et al., Eur. Phys. J. A 43, 45 (2010).

<sup>[10]</sup> C.W. Beqausang et al., Nucl. Instrum. and Methods Phys. Res. A 313, 37 (1992).

<sup>[11]</sup> M. Leino et al., Nucl. Instrum. and Methods Phys. Res. B 99, 653 (1995).

<sup>[12]</sup> M. Leino et al., Nucl. Instrum. and Methods Phys. Res. B 126, 320 (1997).

- [13] R.D. Page et al., Nucl. Instrum. and Methods Phys. Res. B 204, 634 (2003).
- [14] I.H. Lazarus et al., IEEE Trans. Nucl. Sci. 48, 567 (2001).
- [15] P. Rahkila, Nucl. Instrum. and Methods Phys. Res. A **595**, 637 (2008).
- [16] D.C. Radford, Nucl. Instrum. Methods Phys. Res. A361, 297 (1995).
- [17] W. Andrejtscheff et al., Z. Phys. A 328, 23 (1987).
- [18] P. Singh, R.G. Pillay, J.A. Sheikh, and H.G. Devare, Phys. Rev. C 45, 2161 (1992).
- [19] D. Jerrestam *et al.*, Phys. Rev. C **52**, 2448 (1995).
- [20] P.H. Regan et al., Nucl. Phys. **A586**, 351 (1995).
- [21] R. Wadsworth et al., Phys. Rev. Lett. 80, 1174 (1998).
- [22] H. Schnare et al., Phys. Rev. C 54, 1598 (1996).
- [23] E.S. Paul et al., Phys. Rev. C 61, 064320 (2000).
- [24] A. V. Afanasjev and I. Ragnarsson, Nucl. Phys. **A591**, 387 (1995).
- [25] R. Wadsworth et al., Nucl. Phys. **A559**, 461 (1993).
- [26] S. Cwiok et al., Comp. Phys. Commun. 46, 379 (1987).
- [27] W. Satula, R. Wyss, Phys. Scr. T **56**, 159 (1995).
- [28] W. Satula, R. Wyss, P. Magierski, Nucl. Phys. A578, 45 (1994).
- [29] Y. Nogami, H.C. Pradhan, J. Law, Nucl. Phys. A201, 357 (1973).
- [30] J.-y. Zhang, N. Xu, D. B. Fossan, Y. Liang, R. Ma, and E. S. Paul, Phys. Rev. C 39, 714 (1989).
- [31] B. G. Carlsson, and I. Ragnarsson, Phys. Rev. C 74, 011302(R) (2006).